Active Plasma Lensing for Relativistic Laser-Plasma-Accelerated Electron Beams

J. van Tilborg,[1] S. Steinke,[1] C. G. R. Geddes,[1] N. H. Matlis,[1] B. H. Shaw,[1,2] A. J. Gonsalves,[1] J. V. Huijts,[1]
K. Nakamura,[1] J. Daniels,[1] C. B. Schroeder,[1] C. Benedetti,[1] E. Esarey,[1] S. S. Bulanov,[1] N. A. Bobrova,[3]
P. V. Sasorov,[4] and W. P. Leemans[1,2]

[1]*Lawrence Berkeley National Laboratory, University of California, Berkeley, California 94720, USA*
[2]*Department of Physics, University of California, Berkeley, California 94720, USA*
[3]*Institute of Theoretical and Experimental Physics, Moscow 117218, Russia*
[4]*Keldysh Institute of Applied Mathematics, Moscow 125047, Russia*
(Received 8 June 2015; published 28 October 2015)

Compact, tunable, radially symmetric focusing of electrons is critical to laser-plasma accelerator (LPA) applications. Experiments are presented demonstrating the use of a discharge-capillary active plasma lens to focus 100-MeV-level LPA beams. The lens can provide tunable field gradients in excess of 3000 T/m, enabling cm-scale focal lengths for GeV-level beam energies and allowing LPA-based electron beams and light sources to maintain their compact footprint. For a range of lens strengths, excellent agreement with simulation was obtained.

Laser-plasma accelerators (LPAs) [1] have produced MeV-to-multi-GeV electron beams in mm-to-cm-scale plasma structures [2–9]. This maturing technology is being developed for use in applications such as ultrafast electron-beam pump-probe studies [10], compact light sources including coherent x rays [11–13] and incoherent MeV photons [14–17], and high-energy particle colliders driven by multiple LPA stages [18,19]. For all of these, transport and focusing of electron beams over short, cm-scale distances is important. Traditional magnetic elements are challenging to apply: (i) Because of the $1/\gamma^2$ scaling of the focusing strength, with γ the electron relativistic Lorentz factor, solenoids have weak focusing for relativistic electrons and have, hence, only been applied to energies of a few MeV or less [20]; (ii) the strong field gradients of miniature quadrupoles (of order 500 T/m [21]) are promising, as is the more favorable $1/\gamma$ scaling of the focusing strength, but the effective field gradient is strongly reduced when one considers that three lenses of varying and opposite strengths need to be combined to achieve radially symmetric focusing [22]. This leads to a longer effective focal length (of order > tens of cm) with increased chromaticity.

This Letter describes recent multistage LPA experiments where we have realized strong, single-element, radially symmetric focusing of electron beams by applying a discharge current in a gas-filled capillary. Figure 1(a) illustrates the radial focusing force on an electron propagating collinearly to an externally driven discharge current. Such a lens is also referred to as an active plasma lens. Active plasma lenses were first discussed by Panofsky and Baker in 1950 [23], and have been extensively demonstrated on ion beams using z-pinch plasma discharges [24–26]. Until now, applications for electron beams have received little experimental attention. Figure 1(b) highlights the advantage of the active plasma lens, which can provide field gradients > 3000 T/m

for typical parameters considered here. The focal length F_0 for 300-MeV electrons is compared for a state-of-the-art solenoid, quadrupole triplet, and active plasma lens, with values of, respectively, 500, 20, and 1.7 cm. The chromatic dependence can be expressed as the energy-dependent change in focal length $|\Delta F|$ relative to F_0, as shown in Fig. 1(b), and is much weaker for the shorter focal length of the active plasma lens (red curve). Note that plasma-wakefield lenses, where focusing wakefields are driven by either the electron beam itself [27–30] or a laser pulse [31,32], have been considered for their ultrastrong focusing fields, approaching even 1 T/μm [28]. However, their applicability is challenging since the focusing force has an intrinsic longitudinal variation (electrons in the head of the beam experience a different lens strength than the electrons in the tail), and tunability is limited since electron-beam parameters (charge, current profile, and size) strongly affect the focusing forces and lens aberrations.
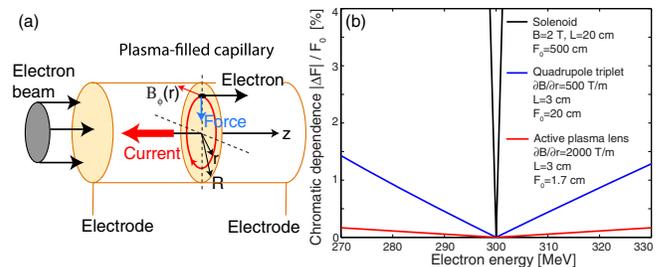
FIG. 1 (color online). (a) Schematic concept of the focusing force in an active plasma lens. (b) The focal length F_0 for 300-MeV electrons and chromatic dependency $|\Delta F/F_0|$ is displayed for a state-of-the-art solenoid (black curve), quadrupole triplet (blue curve), and active plasma lens (red curve), illustrating the advantage of the active plasma lens (cm-scale focal length with reduced chromatic dependence).

Here, we present experimental results of sapphire-based capillary discharges as active plasma lenses. LPA-produced electrons at 100-MeV-level energies with a broad energy spread were used to characterize the focusing capabilities and chromatic effects. The lens strength is varied over a large range, up to field gradients where the electron beam undergoes multiple oscillations within the lens. Energy-integrated and energy-dispersed beam-size measurements are presented, with field gradients up to $\simeq 3500$ T/m demonstrated. Excellent agreement between data and transport simulations is retrieved.

The capillary-discharge plasma channel typically consists of a few-cm hollow tube of diameter 250–1000 μm laser machined into a sapphire substrate [33,34], see Fig. 2. Two gas-inlet slots fill the capillary with H_2 gas at pressures of order 10–200 Torr (6×10^{17}–1×10^{19} electrons/cm^3). Two electrodes are placed on each end to provide a voltage differential. Following the breakdown of the gas by a 15–30-kV pulser system, a strong sub-μs current pulse flows axially through the capillary. A representative measured current trace for a 250-μm-diameter capillary at 26 kV is shown in Fig. 3(a). Magnetohydrodynamics (MHD) simulations showed [35] that after the maximum of the current pulse, the plasma is fully ionized and is in quasiequilibrium. In this case, the current is distributed approximately uniformly within the capillary aperture, and can be expressed as $J = I_0/(\pi R^2)$, with I_0 the peak current and R the capillary radius. The magnetic field B_ϕ within the aperture ($r < R$) can then be derived from Ampère's law to be $B_\phi = \mu_0 J r/2$ and

$$\partial B_\phi/\partial r = \mu_0 I_0/(2\pi R^2), \tag{1}$$

with μ_0 the vacuum permeability. For currents of order 300 A, B_ϕ exceeds 0.2 T, with the field gradient $\partial B_\phi/\partial r$ surpassing 3000 T/m. The validity of the assumption of uniform J is highlighted in Fig. 3(b), which displays $B_\phi(r)$ as obtained from MHD simulations similar to Ref. [35], based on $R = 125$ μm, 150 Torr H_2, $T = 0$ ns, and $I_0 = 330$ A. In this example, a constant gradient is maintained up to $R/2$, with a roll-off at larger radii. First, we will work with the assumption of a constant field gradient, which well characterizes the region $r < R/2$ and allows for

analytic expressions to capture the essential transport behavior. Note that wakefield focusing effects in the active plasma lens, self-driven by the electron beam, can be neglected if $(\sigma_z/\sigma)^2 n_b/n_0 \ll 2(I_0/I_A)(k_p R)^{-2}$, with σ_z the rms beam length, σ the rms transverse beam size, $k_p = \sqrt{n_0 e^2/m_0 c^2 \varepsilon_0}$ the plasma wave number (with e the electronic charge, ε_0 the vacuum permittivity, m_0 the electron rest mass, and n_0 the plasma electron density), $n_b = (Q/e)/[(2\pi)^{3/2}\sigma_z\sigma^2]$ the beam density (assuming a bi-Gaussian distribution), Q the beam charge, and $I_A = 4\pi\varepsilon_0 m_0 c^3/e \simeq 17$ kA the Alfvén current. This condition assumes that $k_p\sigma \gg 1$, $k_p\sigma_z \ll 1$, and $n_b < n_0$. For the electron-beam parameters ($Q = 30$ pC, $\sigma_z = 2$ μm, and $\sigma = 100$ μm) and lens parameters ($n_0 = 10^{18}$ cm^{-3}, $R = 125$ μm, and $I_0 = 300$–3000 A) considered, this condition is well satisfied. However, self-driven wakefields could limit application of active lenses for higher-charge and resonant electron beams.

The electron-beam lens can be described by strength parameter $k = e(\partial B_\phi/\partial r)/(m_0\gamma c)$. The thin-lens approximation yields a focal length of $f = 1/(kL)$, which represents the effective focal length F in both the x and y directions [see the red curve in Fig. 1(b)]. The same expression $f = \pm m_0\gamma c/[eL(\partial B_\phi/\partial r)]$ can be used for a quadrupole, with opposite strength signs in the transverse directions. To compare to the radially symmetric triplet configuration, we follow the optimized configuration $\pm(2f, -f, f)$ of Ref. [36], where each quadrupole is separated by distance $s = f_0$, with f_0 the single-element focal length at the specific design energy [300 MeV in Fig. 1(b)]. To capture the triplet footprint impact, we define the effective focal length F as the distance for a parallel input beam from the first lens to the waist, yielding $F = 2s + (2f^3 - fs^2)/(f^2 + fs - s^2)$. F is shown as a blue curve in Fig. 1(b), based on a state-of-the-art $\partial B_\phi/\partial r = 500$ T/m [21]. The focal length for a radially symmetric solenoid lens [36] is $F = f = (2m_0\gamma c/e)^2/(B^2 L)$ [the black curve in Fig. 1(b) for $B = 2$ T and $L = 20$ cm]. One can observe that the active plasma has the shortest focal length, which yields the weakest energy dependence.

FIG. 2 (color online). Schematic of the jet-based LPA with active plasma lens. A thin tape is spooled every laser shot in order to protect the capillary from remnant laser light. Energy-integrated (from the phosphor screen) and energy-dispersed (from the magnetic spectrometer) beam-size measurements are recorded.
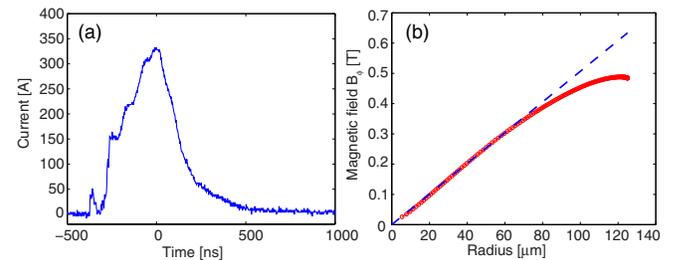
FIG. 3 (color online). (a) Current trace for the sapphire-based capillary discharge. (b) Scaling of the magnetic field with radius as obtained from MHD simulations at $I_0 = 330$ A (solid curve). Linear field gradients (dashed curve) are observed to be linear up to $R/2$, with R the capillary radius (125 μm in this case).

To experimentally demonstrate active plasma lensing on a relativistic LPA-produced electron beam, the setup as depicted in Fig. 2 was operated at LBNL's BELLA Center. A 1.3-J laser was focused by a parabola with 2-m focal length to a spot size of $w_0 = 22$ μm onto a de Laval gas jet of 700 μm diameter. At jet pressures of 140 psi (a mixture of 99% He, 1% N_2), electrons of energy 100 MeV and 30% rms energy spread were produced. A 15-μm, thick Mylar tape was placed 1.5 cm from the LPA in order to reflect remnant laser light while transmitting the electron beam [37]. Following the tape, the electron beam traveled 2 cm to the active plasma lens. The latter was a laser-machined sapphire-based cylindrically symmetric structure of length 33 mm and radius 125 μm. At 150 Torr, the plasma density was estimated to be $\simeq 7 \times 10^{18}$ cm^{-3} based on pressure measurements and MHD simulations [33,38]. The current trace through the capillary is shown in Fig. 3(a). After the active plasma lens, the electron beam propagated 1.7 m to a removable phosphor screen for energy-integrated charge distribution measurements, followed by 1 m of propagation to a phosphor-screen-based magnetic spectrometer. The spatial resolution of the phosphor screens was estimated to be 0.2 mm (rms), while relevant properties of the magnetic spectrometer (i.e., energy resolution and fringe fields) were described in Ref. [39]. Although the divergence was of order 2 mrad (rms), the angular acceptance of the capillary exit limited the tape-affected throughput to ± 1.6 mrad.

By scanning the arrival time of the electron beam with respect to the discharge pulse (peak current of 300 A), the focusing force of the active plasma lens was varied. Figure 4(a) displays a single-shot transverse charge distribution in the absence of a discharge current. The beam size is $\sigma = 2.8$ mm (1.6 mrad), which is consistent with projecting the 125-μm-radius capillary exit at 6.8 cm from the LPA source onto the screen (note the softened edges from the capillary exit truncation). At an arrival time of 350 ns after the peak of the discharge, the current was 45 A and the electron beam was measured to reach its smallest size, with $\sigma = 0.9$ mm (0.53 mrad), as shown in Fig. 4(b). This representative image shows that the lens can deliver a circularly symmetric beam to the target plane. The pointing fluctuation for 20 consecutive shots was 0.35 mm in the x
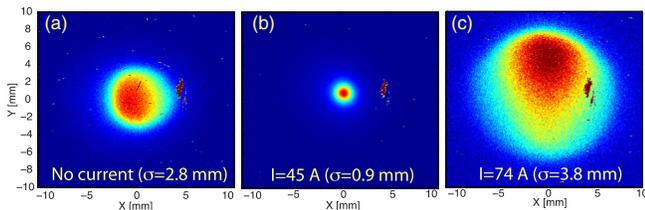
direction and 0.33 mm in the y direction. The lens produced a diverging electron beam for a current of 74 A, see Fig. 4(c), yielding $\sigma = 3.8$ mm (2.2 mrad), indicating a focal location upstream of the phosphor screen (overfocusing).

By removing the phosphor screen, see Fig. 2, the electron beam was transported to the magnetic spectrometer. A timing scan was performed, with the electron beam scanned from arrival prior to the discharge pulse [Fig. 5(a), top] to later than the discharge current peak [Fig. 5(a), bottom]. The vertical acceptance of the magnetic spectrometer is ± 6.0 mm (± 2.2 mrad). In order to provide insight into the observations, we modeled the transport from the LPA source to the spectrometer at each timing, see Fig. 5(b). The model was based on calculating the electron-beam Twiss parameters $(\alpha_T, \beta_T, \gamma_T)$ from the appropriate transport matrices [40]. We followed Ref. [40] to derive the electron-atom scattering in the tape ($\theta_s = 0.9$ mrad) and updated the Twiss parameters accordingly (the scattering increased the emittance ϵ to $\epsilon\sqrt{1 + \xi}$, with $\xi = \theta_s^2 \beta_T / \epsilon$). The simulations were based on a Gaussian energy spectrum at 100 MeV and a spread of 30 MeV (rms), similar to the experiments. Because of experimental fluctuations in charge and energy distribution, we have normalized the color scale for each image in Fig. 5(a) to unity, and have chosen the color scale for each image in Fig. 5(b) to provide qualitative color matching to its corresponding experimental image. The divergence used in the model was 2 mrad, and we excluded particles that cross the capillary wall. With $\theta_s = 0.9$ mrad, one can show that for LPA emittances of a few nm or less (source size a few μm or less), the post-tape

FIG. 4 (color online). Single-shot images of the transverse charge distribution as obtained by the energy-integrated phosphor screen. Relative to the lens-off case in (a), the electron beam is (b) focused (converging) to a smaller size at $I_0 = 45$ A and (c) overfocused (diverging) to a larger size at 74 A.
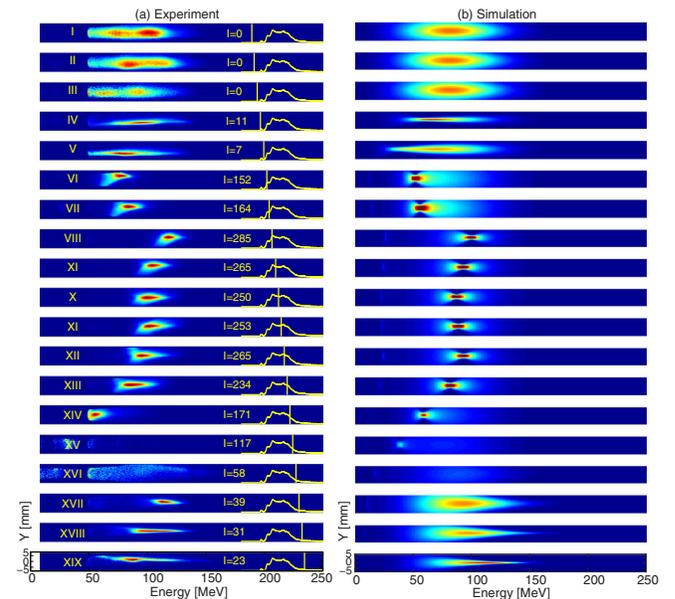
FIG. 5 (color online). Comparison between single-shot experimental (a) and simulated (b) magnetic spectrometer images during a scan of the timing of the electron beam with respect to the discharge pulse. The yellow insets in (a) display the timing of the electron beam as vertical lines.

emittance is dominated by scattering in the tape. Therefore, although we used a LPA source size of 2 μm for the simulations (consistent with previous LPA measurements [41,42]), our calculation results are equally consistent with any chosen source size $\lesssim 5$ μm. To provide qualitative insight, the simulations in Fig. 5(b) are based on a linear profile $B_\phi(r) \propto r$ and have not been corrected for resolution effects. Note that the simulations relied on a Gaussian energy spectrum, an energy-independent divergence, and on-axis pointing. These simplifications form the basis for some of the observed remnant discrepancies. For example, the measured energy spectrum contains a substructure in the form of a (fluctuating) double-Gaussian distribution, and can have a more abrupt high-energy cutoff. Furthermore, electron-beam pointing fluctuations through the lens lead to astigmatism at the image plane, manifesting itself as a tilted or curved bow tie (causing part of the spectrum to be outside of the detector acceptance). Also, due to a strong LPA-driven electromagnetic pulse picked up by the current-measuring oscilloscope, the actual and recorded current deviate slightly, causing a minor discrepancy between the measured and simulated focused energy. As Figs. 5(a) and 5(b) indicate, good qualitative agreement to the simulations was obtained.

In the absence of a discharge current [see Fig. 5(a) I–III], the electron beam did not experience a radial force. Each energy bandwidth was transported with equal transmission, while, transversely, the electron beam was overfilling the magnetic spectrometer. As the current was increased to the level of 5–40 A [see Fig. 5(a) IV–V and 5(a) XVII–XIX], electrons in the range 50–130 MeV experienced focusing onto the magnetic spectrometer with weak chromaticity. At 40–150 A the electron beam was overfocused [in agreement with a well-focused beam on the closer phosphor screen at $I_0 = 45$ A in Fig. 4(b)] and the energy transmission dropped to near zero [see Fig. 5(a) XV–XVI]. However, at even higher currents [200–300 A, see Fig. 5(a) VI–XIV] a revival was seen, where the electron beam was focused following an extra oscillation inside the plasma lens.

To compare experiments to simulation in a more quantitative manner (including the nonlinear radial magnetic field distribution), we first consider a representative single-shot magnetic spectrometer image obtained at a plasma lens current of 23 A [see Fig. 6(a), top]. Data analysis (red circles) reveals a minimum beam size of $\sigma = 0.81$ mm at 110 MeV, with a weak chromatic dependency; electrons from 80 to 140 MeV have a beam size less than 2.0 mm. The solid blue curve in Fig. 6(a) shows the simulated dispersed beam size.

The simulations shown in Fig. 6 were obtained as follows: (i) Based on the Twiss parameter description, we propagated the electron beam from the LPA source to the tape, after which the effects of tape-induced scattering were included. The transport and scattering yielded a new effective source location, source size, and source
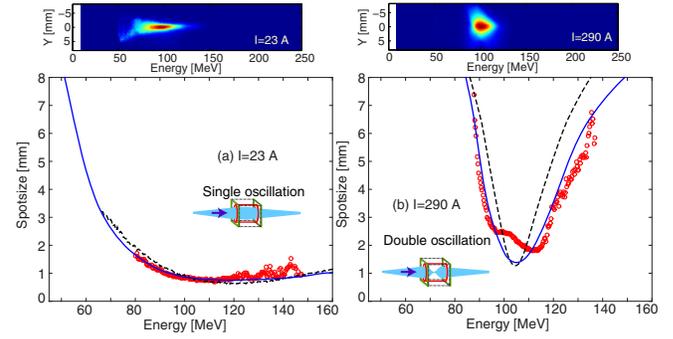
FIG. 6 (color online). Data (red circles) on the transverse electron-beam size σ are compared to simulation ($\sigma_{\mathrm{sim,final}}$, solid blue curve) in case of a weak focusing current in (a), where the electron beam is well focused by the active plasma lens, and in case of a stronger focusing current in (b), where an extra oscillation within the lens yields a much stronger chromatic dependency. The black dashed curves display simulation results assuming uniform current density ($B_\phi \propto r$) and perfect resolution.

divergence. (ii) Starting from this effective source, we then shifted to a particle tracking approach. Test particles were transported from the effective source to the active plasma lens entrance, through the lens, and to the magnetic spectrometer. To include the nonlinear radial magnetic field profile based on the simulation results of Fig. 3(b), we replaced I_0 in Eq. (1) by $I_0(1 - \rho r^2)$, with $\rho = 6.5 \times 10^7$ m^{-2}. Statistical analysis at the simulated magnetic spectrometer plane was convoluted with the (minor) contributions from spectrometer's spatial and energy resolution. At each energy E, the transverse distribution was described by a Gaussian of width σ_{sim}. The simulation curve of σ_{sim} [solid blue curve in Fig. 6(a)] shows good agreement with the data.

We repeated the comparison to simulation for the experimental data obtained at a larger plasma lens current [290 A, see Fig. 6(b)], where the electron beam performed a double oscillation before exiting the lens. The optimum electron energy for transport onto the magnetic spectrometer was 102 MeV. Because of the double oscillation, the chromatic dependency on the lens strength is now much stronger, resulting in a steeper beam-size increase at nearby energies [red circles in Fig. 6(b)]. Following the same resolution considerations, we again observe good agreement between the data and simulation. The remaining discrepancy may be due to nonuniform current distributions and electron-beam alignment imperfections. The simulations were repeated (see black dashed curves) assuming uniform density $B_\phi \propto r$ at optimum energy resolution, highlighting the small but observable relevance of the nonuniform current distribution. Because of the uncertainty ($\lesssim 10$ A) in the measured current, we have varied the simulation current to match the measured focused electron energy. Note that for multi-percent energy-spread transport applications one would tune the current to operate in the single-oscillation regime [see the

solid red simulation curve in Fig. 1(b) and experimental data in Fig. 6(a)].

In conclusion, we have presented an experimental characterization of the use of a discharge-capillary active plasma lens to transport 100-MeV-level electron beams produced by a laser-plasma accelerator. The plasma lenses can have field gradients in excess of 3000 T/m, allowing for the focusing of GeV-level electron beams over distances of a few cm. Such a strong lens could be relevant for LPA applications where compactness and tunability are critical (e.g., LPA-based light sources, multistage acceleration, Thomson scattering, or electron-beam pump-probe studies). By changing the magnetic field strength, we showed focusing with weak chromatic dependencies and (after an extra oscillation at higher currents) with stronger chromatic dependencies. By incorporating the spatial and energy resolution of the magnetic spectrometer, excellent agreement of the data to simulation was retrieved. The electron-beam size at the optimum focused energy was 0.81 mm (rms), dominated by the emittance degradation of the LPA electron beam in the laser-blocking tape. This is consistent with an upper-bound LPA geometrical emittance of $\lesssim 7$ nm (source size $\lesssim 5$ μm).

[1] E. Esarey, C. B. Schroeder, and W. P. Leemans, Rev. Mod. Phys. **81**, 1229 (2009).

[2] J. Faure, Y. Glinec, A. Pukhov, S. Kiselev, S. Gordienko, E. Lefebvre, J.-P. Rousseau, F. Burgy, and V. Malka, Nature (London) **431**, 541 (2004).

[3] C. G. R. Geddes, Cs. Toth, J. van Tilborg, E. Esarey, C. B. Schroeder, D. Bruhwiler, C. Nieter, J. Cary, and W. P. Leemans, Nature (London) **431**, 538 (2004).

[4] S. P. D. Mangles *et al.*, Nature (London) **431**, 535 (2004).

[5] W. P. Leemans, B. Nagler, A. J. Gonsalves, Cs. Tóth, K. Nakamura, C. G. R. Geddes, E. Esarey, C. B. Schroeder, and S. M. Hooker, Nat. Phys. **2**, 696 (2006).

[6] C. E. Clayton *et al.*, Phys. Rev. Lett. **105**, 105003 (2010).

[7] H. T. Kim, K. H. Pae, H. J. Cha, I. J. Kim, T. J. Yu, J. H. Sung, S. K. Lee, T. M. Jeong, and J. Lee, Phys. Rev. Lett. **111**, 165002 (2013).

[8] Xiaoming Wang *et al.*, Nat. Commun. **4**, 1988 (2013).

[9] W. P. Leemans *et al.*, Phys. Rev. Lett. **113**, 245002 (2014).

[10] I. Tudosa, C. Stamm, A. B. Kashuba, F. King, H. C. Siegmann, J. Stöhr, G. Ju, B. Lu, and D. Weller, Nature (London) **428**, 831 (2004).

[11] A. R. Maier, A. Meseck, S. Reiche, C. B. Schroeder, T. Seggebrock, and F. Grüner, Phys. Rev. X **2**, 031019 (2012).

[12] C. B. Schroeder *et al.*, in *Proceedings of FEL 2013* (JACoW, New York, NY, 2013), http://www.JACoW.org.

[13] M. E. Couprie, A. Loulergue, M. Labat, R. Lehe, and V. Malka, J. Phys. B **47**, 234001 (2014).

[14] Y. Glinec *et al.*, Phys. Rev. Lett. **94**, 025003 (2005).

[15] S. Chen *et al.*, Phys. Rev. Lett. **110**, 155003 (2013).

[16] N. D. Powers, I. Ghebregziabher, G. Golovin, C. Liu, S. Chen, S. Banerjee, J. Zhang, and D. P. Umstadter, Nat. Photonics **8**, 28 (2013).

[17] S. G. Rykovanov, C. G. R Geddes, J.-L. Vay, C. B. Schroeder, E. Esarey, and W. P. Leemans, J. Phys. B **47**, 234013 (2014).

[18] W. P. Leemans and E. Esarey, Phys. Today **62**, No. 3, 44 (2009).

[19] S. Steinke *et al.*, in *Proceedings of Advanced Accelerator Concepts Workshop* (AIP, San Jose, CA, 2014), http://scitation.aip.org.

[20] Z.-H. He, A. G. R. Thomas, B. Beaurepaire, J. A. Nees, B. Hou, V. Malka, K. Krushelnick, and J. Faure, Appl. Phys. Lett. **102**, 064104 (2013).

[21] R. Weingartner *et al.*, Phys. Rev. ST Accel. Beams **14**, 052801 (2011).

[22] J. K. Lim, P. Frigola, G. Travish, J. B. Rosenzweig, S. G. Anderson, W. J. Brown, J. S. Jacob, C. L. Robbins, and A. M. Tremaine, Phys. Rev. ST Accel. Beams **8**, 072401 (2005).

[23] W. K. H. Panofsky and W. R. Baker, Rev. Sci. Instrum. **21**, 445 (1950).

[24] E. Boggasch, J. Jacoby, H. Wahl, K.-G. Dietrich, D. H. H. Hoffmann, W. Laux, M. Elfers, C. R. Haas, V. P. Dubenkov, and A. A. Golubev, Phys. Rev. Lett. **66**, 1705 (1991).

[25] B. Autin, H. Riege, E. Boggasch, K. Frank, L. de Menna, and G. Miano, IEEE Trans. Plasma Sci. **15**, 226 (1987).

[26] F. Dothan, H. Riege, E. Boggasch, and K. Frank, J. Appl. Phys. **62**, 3585 (1987).

[27] R. Govil, W. P. Leemans, E. Y. Backhaus, and J. S. Wurtele, Phys. Rev. Lett. **83**, 3202 (1999).

[28] J. S. T. Ng *et al.*, Phys. Rev. Lett. **87**, 244801 (2001).

[29] P. Muggli *et al.*, Phys. Rev. Lett. **101**, 055001 (2008).

[30] M. C. Thompson *et al.*, Phys. Plasmas **17**, 073105 (2010).

[31] R. Lehe, C. Thaury, E. Guillaume, A. Lifschitz, and V. Malka, Phys. Rev. ST Accel. Beams **17**, 121301 (2014).

[32] C. Thaury *et al.*, Nat. Commun. **6**, 6860 (2015).

[33] A. J. Gonsalves, T. P. Rowlands-Rees, B. H. P. Broks, J. J. A. M. van der Mullen, and S. M. Hooker, Phys. Rev. Lett. **98**, 025002 (2007).

[34] J. van Tilborg, J. Daniels, A. J. Gonsalves, C. B. Schroeder, E. Esarey, and W. P. Leemans, Phys. Rev. E **89**, 063103 (2014).

[35] N. A. Bobrova, P. V. Sasorov, C. Benedetti, S. S. Bulanov, C. G. R. Geddes, C. B. Schroeder, E. Esarey, and W. P. Leemans, Phys. Plasmas **20**, 020703 (2013).

[36] I. Hofmann, Phys. Rev. ST Accel. Beams **16**, 041302 (2013).

[37] B. H. Shaw, J. van Tilborg, T. Sokollik, C. B. Schroeder, W. R. McKinney, N. A. Artemiev, V. V. Yashchuk, E. M. Gullikson, and W. P. Leemans, J. Appl. Phys. **114**, 043106 (2013).

[38] N. A. Bobrova (private communication).

[39] K. Nakamura, W. Wan, N. Ybarrolaza, D. Syversrud, J. Wallig, and W. P. Leemans, Rev. Sci. Instrum. **79**, 053301 (2008).

[40] M. B. Reid, J. Appl. Phys. **70**, 7185 (1991).

[41] R. Weingartner *et al.*, Phys. Rev. ST Accel. Beams **15**, 111302 (2012).

[42] G. R. Plateau *et al.*, Phys. Rev. Lett. **109**, 064802 (2012).